

Article

Mn-doped CeO₂ Nanorod Supported Au Catalysts for Dehydrogenation of Ethane with CO₂

Tianqi Lei ¹, Hongyao Guo ¹, Changxi Miao ², Weiming Hua ¹, Yinghong Yue ^{1,*} and Zi Gao ¹

¹ Department of Chemistry, Shanghai Key Laboratory of Molecular Catalysis and Innovative Materials, Fudan University, Shanghai 200438, China; leitianqi90@126.com (T.L.); guohongyao@163.com (H.G.); wmhua@fudan.edu.cn (W.H.); zigao@fudan.edu.cn (Z.G.)

² Shanghai Research Institute of Petrochemical Technology, Shanghai 201208, China; miaocx.sshy@sinopec.com

* Correspondence: yhyue@fudan.edu.cn; Tel.: +86-21-31249120

Received: 15 January 2019; Accepted: 27 January 2019; Published: 30 January 2019



Abstract: Dehydrogenation of ethane to ethylene was investigated in the presence of CO₂ over Au catalyst supported on an Mn-doped ceria nanorod. The activity can be greatly enhanced by proper Mn doping. Mn was found to preferentially occupy defect sites or surface sites of ceria, resulting in the formation of extra oxide ions. Characterization results indicated that the reducible oxygen species related to ceria might play a vital role in the dehydrogenation. The addition of CO₂ improved the stability of the catalysts remarkably, since CO₂ can sustainably replenish the reducible oxygen species and eliminate the coke on the surface of the catalysts, which was proved by the H₂-TPR and Raman analysis of spent catalysts. An ethane conversion of 17.4% with an ethylene selectivity of 97.5% can be obtained after 44 h of reaction.

Keywords: Ethane dehydrogenation; Au catalyst; Mn-doping; CeO₂ nanorod; CO₂

1. Introduction

Being one of the most important types of compounds in the chemical industry, ethylene can be extensively used as feedstock for producing polyethylene, ethylene oxide, ethylene glycol, vinyl chloride, acetaldehyde, acetic acid and other derivatives. The catalytic dehydrogenation of ethane to ethylene has drawn intense attention due to the increasing demand for replacing the utilization of petroleum with nature gas and shale gas [1,2]. Compared with direct alkane dehydrogenation, oxidative dehydrogenation with CO₂ is more advantageous because higher equilibrium conversion and lower carbon deposits can be achieved via reverse water-gas shift reaction (RWGS) and Boudouard reaction [3–6].

The dehydrogenation of light paraffins in the presence of CO₂ has been widely researched in the previous decade. Cr₂O₃- and Ga₂O₃-based catalysts are reported to be more active than others for the reaction [7–11]. Nevertheless, these kinds of catalysts are still limited by the drawbacks of environmental hostility, relatively low selectivity or poor long-term stability. Recently, the reaction between ethane/propane and CO₂ has been studied on Au-based catalysts [12,13]. Dry reforming as well as oxidative dehydrogenation can occur over these supported Au catalysts. More recent results show that CeO₂-supported Au is an excellent catalyst for oxidative dehydrogenation of ethane with CO₂, and nanorod CeO₂-supported Au exhibits higher activity and better stability than nanoparticle supported one [14]. The surface oxygen reducibility of ceria is found to play a vital role in dehydrogenation.

CeO₂ has been commonly employed as a catalyst or catalyst support for various redox reactions due to its high oxygen storage/release capacities [15–18]. Significant enhancement has been reported

in redox properties as well as catalytic activities by the doping of other transition metal oxides [19, 20], among which manganese oxide (MnO_x) has been proved to be an excellent doping agent for CeO_2 -based catalysts for many redox reactions such as ammonia oxidation, volatile organic compound combustion and CO oxidation [21–23].

In this contribution, Mn-doped CeO_2 nanorod was synthesized and utilized as a support for an Au catalyst. The catalyst was characterized by XRD, TEM, XPS, H_2 -TPR, Raman and N_2 adsorption, and the catalytic performance for the dehydrogenation of ethane to ethylene in the presence of CO_2 was established. The effects of Mn doping and CO_2 addition on the dehydrogenation reaction are also discussed herein on the basis of characterization.

2. Results and Discussion

2.1. Catalyst Characterization

The XRD patterns of $\text{Ce}_{1-x}\text{Mn}_x\text{O}_{2-\delta}$ -supported Au catalysts with various Mn/Ce ratios are illustrated in Figure 1. All the catalysts exhibited only CeO_2 cubic fluorite diffraction peaks ($2\theta = 28.6^\circ$, 33.1° , 47.5° and 56.5° , PDF# 81-0792) without any peaks of manganese oxide phases. A progressive shift to high Bragg angle and width-broadening of the diffraction peaks can also be observed, indicating that the manganese species entered in the CeO_2 lattice and formed $\text{Ce}_{1-x}\text{Mn}_x\text{O}_{2-\delta}$ solid solution [24]. The pure manganese oxide exhibited dominant diffraction peaks at $2\theta = 32.9^\circ$ and 38.2° , which are the characteristics of Mn_2O_3 (PDF#89-4836 /65-1798). No distinct diffraction peak attributed to the Au phase was observed, revealing the high dispersion of the gold species on these supports.

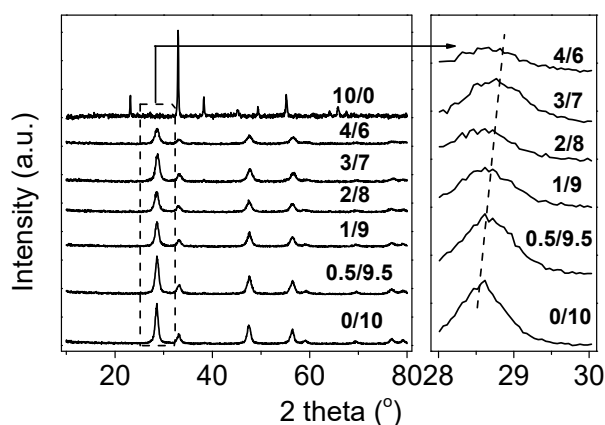


Figure 1. XRD patterns of $\text{Ce}_{1-x}\text{Mn}_x\text{O}_{2-\delta}$ -supported Au catalysts with different Mn/Ce ratios.

The morphologies of the CeO_2 and Mn-doped CeO_2 materials after Au loading were attained by TEM and the images are shown in Figure 2. Au/CeO_2 displayed the morphology of the nanorod, whose diameter is 11.5 ± 1.0 nm and length is in the range of 42 to 65 nm, exactly the same as the results reported before [14]. Previous studies have shown that this CeO_2 nanorod grows along the [110] direction, exposing mostly less stable {001} and {110} crystal planes which gives rise to higher redox activity and better dispersion of Au nanoclusters [25,26]. The doping of Mn did not alter the nanorod morphology of the CeO_2 but led to progressive shortening of the length, in accordance with the widening of the X-ray diffraction peaks. Taking the $\text{Au/Ce}_{0.6}\text{Mn}_{0.4}$ catalyst for example, the length of the nanorod was decreased to 19~32 nm. By contrast, the $\text{Au/Mn}_2\text{O}_3$ catalyst showed no unique morphology, just block mass with much bigger sizes.

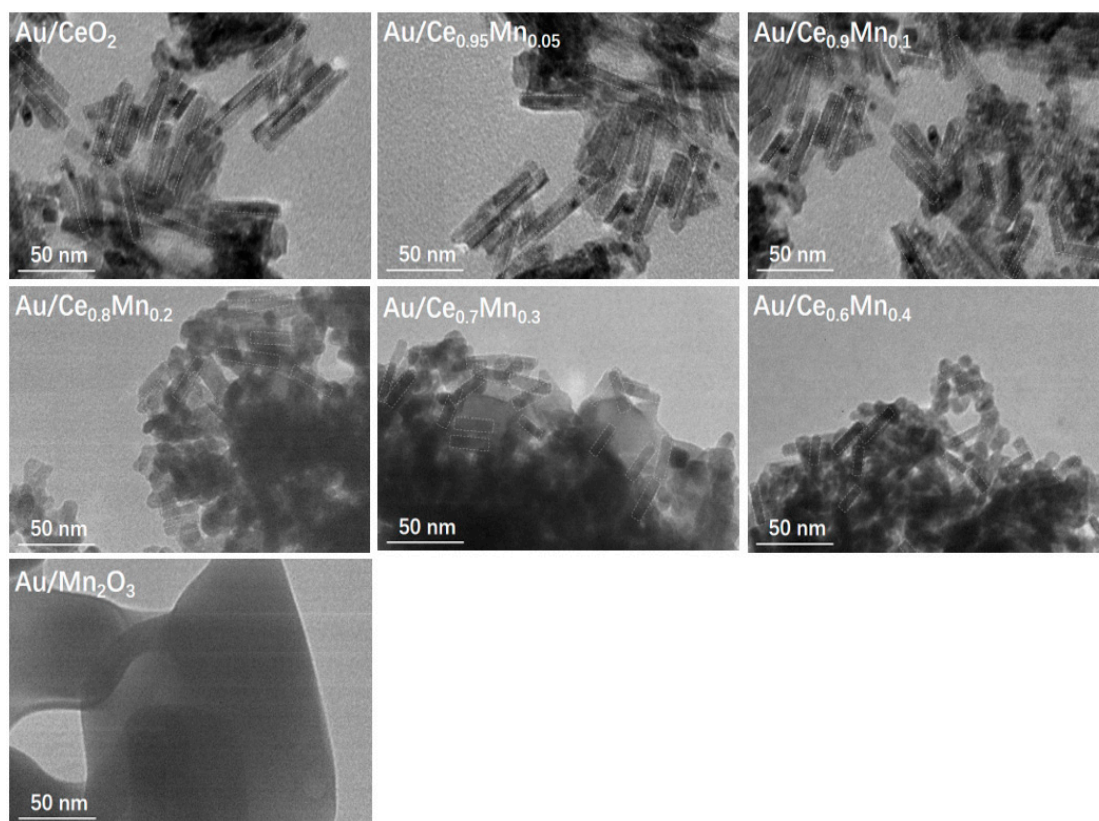


Figure 2. TEM images of the Au/Ce_{1-x}Mn_xO_{2-δ} catalysts with different Mn/Ce ratios.

Textural properties of the catalysts are obtained via N₂ adsorption, and the results are shown in Table 1. The specific surface areas of the CeO₂-based catalysts changed little after the Mn-doping. However, they are much higher than that of the Au/Mn₂O₃ catalyst.

Table 1. Textural and structural properties of the Au/Ce_{1-x}Mn_xO_{2-δ} samples.

Catalysts	S _{BET} (m ² /g)	Ce ³⁺ Percent	Surface Ce/Mn Ratio	Mn ²⁺ in Total Mn (%)
Au/CeO ₂	66	28.0	-	-
Au/Ce _{0.95} Mn _{0.05}	65	16.7	15.8	-
Au/Ce _{0.9} Mn _{0.1}	67	16.5	9.8	-
Au/Ce _{0.8} Mn _{0.2}	62	7.9	4.6	8.0
Au/Ce _{0.7} Mn _{0.3}	59	6.6	3.3	5.3
Au/Ce _{0.6} Mn _{0.4}	62	6.3	1.9	3.4
Au/Mn ₂ O ₃	3	-	-	1.8

The Raman spectra of Au/Ce_{1-x}Mn_xO_{2-δ} catalysts are illustrated in Figure 3. The Au/CeO₂ mainly exhibited a peak at 459 cm⁻¹ due to the ceria F_{2g} active mode. Such a characteristic peak shifted to a lower wavenumber at around 442 cm⁻¹ after the Mn doping, which was caused by the incorporation of Mn ions in the CeO₂ matrix [27,28]. The manganese oxides exhibited a relatively weak Raman peak at around 634 cm⁻¹ which can only be observed in the Ce_{1-x}Mn_xO_{2-δ} samples with high Mn molar ratio ($x > 0.3$) [27,29]. The Au/CeO₂ also exhibited a weak peak at ~268 cm⁻¹ and ~600 cm⁻¹, which is attributed to the oxygen vacancies caused by the presence of Ce³⁺. However, this peak did not appear in all of the Mn-doping samples, indicating the consumption of oxygen vacancies. It was reported that the Mn³⁺, whose ionic radius (58 pm) is much smaller than that of host Ce⁴⁺ (114 pm), seemed to preferentially occupy the surface or defect sites of CeO₂ crystals, causing the disappearance of O²⁻ vacancies and/or the creation of extra oxide ions [27].

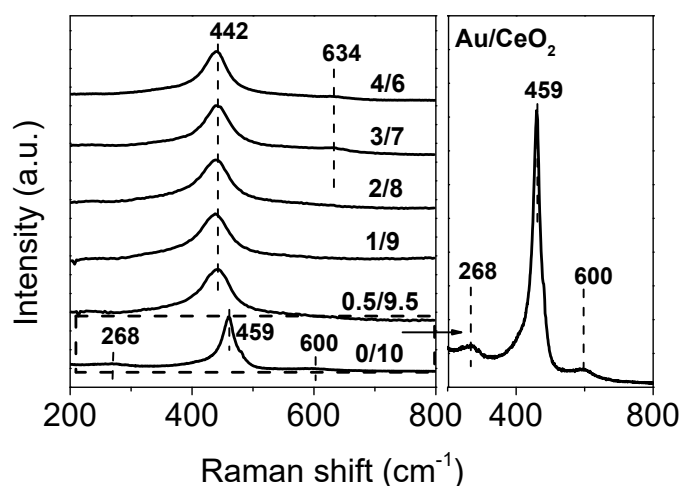


Figure 3. Raman spectra of the Au/Ce_{1-x}Mn_xO_{2-δ} catalysts with different Mn/Ce ratios.

XPS spectra were established to examine the surface composition and chemical states of Ce, Mn and Au, and the results are shown in Figure S1 and Table 1. The surface Ce/Mn ratio is a bit lower than the stoichiometry with low Mn content ($x \leq 0.1$) and becomes higher with increasing Mn content ($x > 0.1$), indicating that the manganese species tended to disperse on the surface firstly and later enriched in the bulk phase. The complex spectra of Ce 3d were numerically fitted with 10 peaks. The six bands labeled as v_0 , v_1 , v_2 , v_0' , v_1' , and v_2' are characteristic of Ce⁴⁺ while the rest labeled as u_0 , u_1 , u_0' , and u_1' are representative of the Ce 3d_{5/2} component of Ce³⁺ [30]. The relative contents of Ce³⁺ were derived from the calculation of the ratio of peak area, which clearly showed that the Ce³⁺ concentration decreased monotonously with the increasing content of Mn, suggesting that the doping of Mn might occupy the defect sites of ceria and thus, increase the oxidation states of surface Ce. This is consistent with the Raman results. The above results are also proved by Mn 2p XPS spectra of the samples which show predominately Mn 2p_{3/2} and Mn 2p_{1/2} peaks at around 641.1 and 652.9 eV corresponding to the Mn³⁺. A small fraction of Mn²⁺ also existed with binding energy at 640.0 and 651.2 eV [20,27]. An increased fraction of Mn²⁺ was existed in the Ce–Mn composite oxides, indicating the electrons are transferred from Ce to Mn for charge compensation since the doping of Mn increased the surface Ce⁴⁺ species in ceria. The Au 4f XPS spectra of the samples are also exhibited in Figure S1. Au/Mn₂O₃ consists of a pair of distinct peaks at around 83.7 and 87.4 eV assigned to metallic Au and additional shoulders at 85.1 and 89.0 eV representing the oxidized surface Au^{δ+} species with much smaller fraction [31]. All the Ce-containing samples exhibit similar Au 4f peaks. However, their intensities were much lower than that of the Au/Mn₂O₃ and cannot be deconvoluted effectively.

2.2. TPR Studies

The redox behavior of Ce_{1-x}Mn_xO_{2-δ}-supported Au materials was determined and the results are presented in Figure 4. Pure ceria often showed two reduction peaks, attributed to reducible surface oxygen and bulk oxygen species, respectively [14]. For the pure manganese oxide, the profiles were featured by two reduction peaks attributed to the reduction of Mn₂O₃ to Mn₃O₄ and further reduction of Mn₃O₄ to MnO according to previous research [32]. Since the reduction peak of those easily reducible ceria species overlapped with the low-temperature reduction peak of the manganese species in the TPR profiles of Au/Ce_{1-x}Mn_xO_{2-δ}, deconvolution was established and is exhibited in Figure S2. The detailed H₂ consumption amount is presented in Table 2. The total H₂ consumption amount of the Au/Ce_{1-x}Mn_xO_{2-δ} was increased proportionally with the increasing Mn doping amount. However, the consumed hydrogen attributed to the ceria species was increased initially, and then decreased with the Mn amount, reaching the maximum value of 0.33 mmol/g over Au/Ce_{0.9}Mn_{0.1}. This is obviously an integrated result because on the one hand the doping of Mn decreased the ceria molar percent in

the composite oxides, while on the other hand, it occupied the defect or surface sites and generated extra oxide ions related to the Ce ions as revealed by the Raman and XPS measurement.

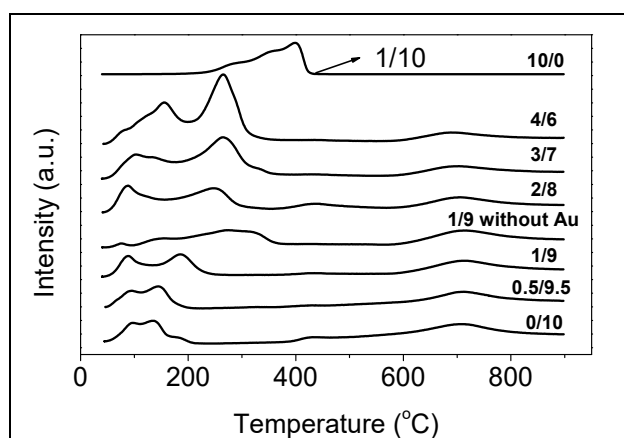


Figure 4. TPR profiles of $Ce_{1-x}Mn_xO_{2-\delta}$ -supported Au catalysts with different Mn/Ce ratios.

Table 2. H_2 -TPR results of the Au-supported catalysts.

Catalysts	Total Reducible Species		Cerium Species
	Temperature (°C)	H_2 Consumption (mmol/g)	H_2 Consumption (mmol/g)
Au/CeO ₂	50–220	0.30	0.30
Au/Ce _{0.95} Mn _{0.05}	50–210	0.36	0.31
Au/Ce _{0.9} Mn _{0.1}	50–270	0.52	0.33
Au/Ce _{0.8} Mn _{0.2}	50–340	0.73	0.28
Au/Ce _{0.7} Mn _{0.3}	50–350	1.02	0.26
Au/Ce _{0.6} Mn _{0.4}	50–350	1.42	0.24
Au/Mn ₂ O ₃	200–430	5.50	-
Au/Ce _{0.9} Mn _{0.1} ¹	50–270	0.24	0.12
Au/Ce _{0.9} Mn _{0.1} ²	50–270	0.23	0.12

¹ Spent catalyst after 6 h; ² spent catalyst after 44 h.

2.3. Catalytic Performance

The dehydrogenation of ethane was conducted in the presence of CO₂ over supported Au catalysts at 650 °C, and the results are shown in Table 3 and Figure 5. Carbon balance was determined by the ratio of the overall hydrocarbon amounts after the reaction to the initial ethane amount. High carbon balance was obtained for all the catalysts investigated, indicating that the dry reforming can be ignored during the reaction. Coke formation always accompanied the dehydrogenation reaction, though the addition of CO₂ was suggested to react with these carbon deposits through the Boudouard reaction. This is probably why the carbon balance here did not reach 100%. Except for coke, all the catalysts exhibit excellent selectivity to the target product ethylene and the only detectable by-product is methane. Although the pure oxide-supported catalysts Au/CeO₂ and Au/Mn₂O₃ showed comparable initial activity, the former exhibited much better stability during the reaction. The ethane conversion of the Au/CeO₂ was maintained with no distinct loss of activity within 6 h of reaction while that of Au/Mn₂O₃ dropped sharply from 16.4% to 4.2%, indicating the different active sites on the two catalysts. Apparently, the ceria-supported Au catalyst is much preferable in the DHE reaction. For Mn-doped CeO₂-supported Au catalysts, the initial ethane conversion was enhanced with the doping of Mn until the Mn/(Ce+Mn) ratio reached 0.1, and then decreased slightly with the further increase of the ratio. Au/Ce_{0.9}Mn_{0.1} achieved the highest initial activity with an ethane conversion of 22.4% and ethylene yield of 22.2%. The initial ethane conversion of Au/Ce_{1-x}Mn_xO_{2-δ} has exactly the same sequence as that of the consumed hydrogen attributing to

the ceria species, indicating that the easily reducible oxygen species related to ceria may play a vital role in the dehydrogenation reaction. Turnover frequency (TOF) was also calculated and compared to that of Ga₂O₃/ZSM-5 and Cr₂O₃/ZSM-5 published before. It seems that Au species are more active than CrO_x or GaO_x species (Table 3).

Table 3. Reaction data in the DHE in the presence of carbon dioxide ¹.

Catalysts	Conversion (%) ²	Selectivity (%) ²		C ₂ H ₄ Yield (%) ²	TOF ⁴ (h ⁻¹)	Carbon Balance (%)
		CH ₄	C ₂ H ₄			
Blank	0.9(0.9)	26.5(25.7)	73.5(74.4)	0.7(0.7)	—	99.3
Au/CeO ₂ [14]	17.2(17.1)	2.4(2.1)	97.6(97.9)	16.8(16.7)	40.8	94.0
Au/Ce _{0.95} Mn _{0.05}	20.4(19.9)	2.0(1.8)	98.0(98.2)	20.0(19.5)	48.4	93.0
Au/Ce _{0.9} Mn _{0.1}	22.7(20.6)	2.0(1.7)	98.0(98.3)	22.2(20.3)	53.9	92.7
Au/Ce _{0.8} Mn _{0.2}	22.4(19.6)	2.3(1.9)	97.7(98.1)	21.9(19.2)	53.2	95.7
Au/Ce _{0.7} Mn _{0.3}	20.2(16.9)	2.1(1.9)	97.9(98.1)	19.8(16.5)	48.0	95.7
Au/Ce _{0.6} Mn _{0.4}	17.3(14.4)	2.2(2.2)	97.8(97.8)	16.9(14.1)	41.1	95.5
Au/Mn ₂ O ₃	16.4(4.2)	1.8(5.5)	98.2(94.5)	16.1(4.0)	38.9	94.2
Ce _{0.9} Mn _{0.1}	10.2(8.8)	3.8(3.3)	96.2(96.7)	9.8(8.5)	—	93.0
Au/CeO ₂ ³ [14]	14.1(1.5)	5.9(19.8)	94.1(80.2)	13.2(1.2)	33.5	95.0
Au/Ce _{0.9} Mn _{0.1} ³	19.4(1.3)	29.8(20.0)	70.2(80.0)	13.6(1.0)	46.1	92.4
Ga ₂ O ₃ /ZSM-5 [9]	25.3(14.6)	6.1(5.4)	91.7(92.0)	23.2(13.4)	5.3	—
Cr ₂ O ₃ /ZSM-5 [10]	65.5(61.3)	24.3(20.9)	75.4(78.9)	49.4(48.4)	20.0	—

¹ Reaction condition: 200 mg catalyst, 650 °C, 3% C₂H₆/15% CO₂ in N₂, flow rate 30 mL/min. ² The values outside and inside the brackets are obtained at 10 min and 6 h, respectively. ³ Reaction condition: 200 mg catalyst, 650 °C, 3% C₂H₆ in N₂, flow rate 30 mL/min. ⁴ Turnover frequency (TOF) was defined for the (reacted C₂H₆ molecules)/(Au, Ga or Cr atoms × time).

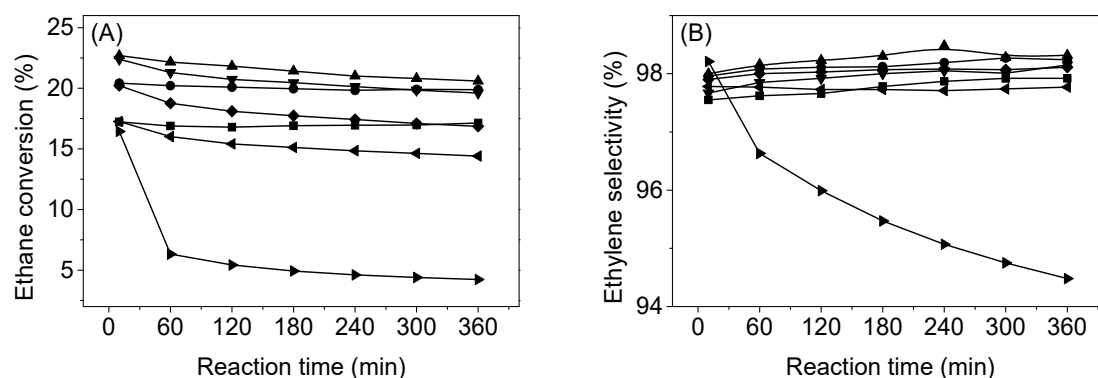


Figure 5. Ethane conversion (A) and ethylene selectivity (B) over various Au catalysts in the presence of CO₂: (■) Au/CeO₂; (●) Au/Ce_{0.95}Mn_{0.05}; (▲) Au/Ce_{0.9}Mn_{0.1}; (▼) Au/Ce_{0.8}Mn_{0.2}; (◆) Au/Ce_{0.7}Mn_{0.3}; (◀) Au/Ce_{0.6}Mn_{0.4}; (▶) Au/Mn₂O₃.

The dehydrogenation of ethane was also conducted over the Ce_{0.9}Mn_{0.1} oxide and the result is also listed in Table 3 for comparison. Though the composite oxide itself also showed some DHE activity with ethane conversion of 10.2 %, it is much lower compared to its gold-loaded counterpart (Au/Ce_{0.9}Mn_{0.1}), revealing the considerable role of Au species in the ethane dehydrogenation over Mn-doped CeO₂ supported Au catalysts. TPR measurements show that the addition of gold can remarkably reduce the temperature of the ceria reduction peak, thus enhancing the reducibility of oxygen species on the catalyst surface [33].

The ethane dehydrogenation over Au/Ce_{0.9}Mn_{0.1} was also investigated in the absence of CO₂ to look into the role of CO₂, and the results are presented in Figure 6 and Table 3. Like Au/CeO₂, the initial activity of Au/Ce_{0.9}Mn_{0.1} was promoted slightly after the addition of CO₂ while the stability was greatly improved. The ethane conversion was decreased sharply with reaction time in the absence of CO₂ and the activity was completely lost within the initial 6 h. However, in the presence of CO₂, over 20% conversion can be maintained during the same period. The promotion effects of CO₂ over

Mn-doped CeO₂ nanorod-supported Au is quite similar as that of unmodified Au/CeO₂ [14], which will be discussed in detail later.

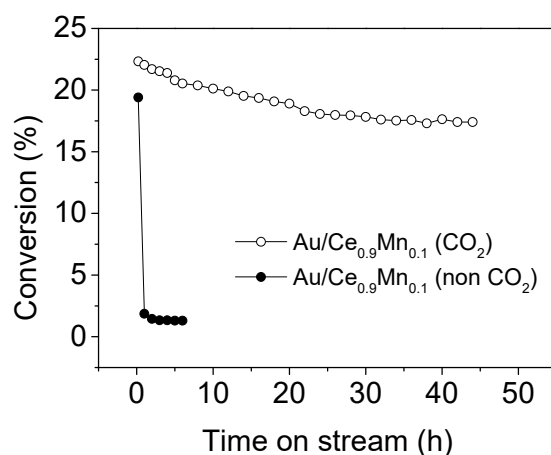


Figure 6. Ethane conversion of long-term dehydrogenation of Au/Ce_{0.9}Mn_{0.1} in the presence and absence of CO₂.

In order to investigate the catalytic stability in more detail, a long-term test was conducted on the Au/Ce_{0.9}Mn_{0.1} catalyst and the results are illustrated in Figure 6. The catalyst deactivated gradually with time on the stream, and finally reaches its steady state after about 30 h. A steady ethane conversion of 17.4% with an ethylene selectivity of 97.5% can be obtained (i.e., TON 41.4, 1 h). It seems that the Au/Ce_{0.9}Mn_{0.1} can become a commercial dehydrogenation catalyst due to its high stability and excellent selectivity.

Coke deposition always acted as the major reason for catalyst deactivation. Raman analysis were performed to elucidate the nature and extent of carbonaceous deposits on the spent Au/Ce_{0.9}Mn_{0.1} catalyst. Peaks at 1324 cm⁻¹ (D band) and 1576 cm⁻¹ (G band) were observed on the spent catalyst after dehydrogenation in the absence of CO₂, which are assigned to disordered carbonaceous species and graphitic carbon, respectively. On the contrary, after dehydrogenation in the presence of CO₂, the identical catalyst exhibited no distinct peaks in that range as shown in Figure S3. This implies that the addition of CO₂ can suppress or eliminate the carbonaceous deposits effectively, which may account for the enhanced stability.

The redox property of spent Au/Ce_{0.9}Mn_{0.1} catalyst was investigated by H₂-TPR, and the results are presented in Figure 7 and Table 2. For the catalyst after dehydrogenation in the presence of CO₂, the TPR profiles are quite similar to that of the fresh one. The low-temperature reduction peak still remained without obvious shifts of peak temperature (still at 50–270 °C), which indicates that their redox properties change little during the reaction. However, its peak intensity was reduced after reaction. The consumed hydrogen attributing to the ceria species decreased from 0.33 mmol/g to 0.12 mmol/g during the initial 6 h, and was maintained at that level even after 44 h of reaction. Since the reducible oxygen species-related CeO₂ were thought to play a crucial role in dehydrogenation, the decrease of these species may account for the partial deactivation of the catalyst. However, after dehydrogenation in the absence of CO₂, the low-temperature peaks had completely disappeared. Some new peaks in the range of 200–400 °C emerged which were different from the inherent low-temperature reduction peaks of CeO₂ oxides. These peaks can be attributed to the hydrogenation of deposited cokes according to the previous reports [34,35]. The loss of these reducible oxygen species is quite reasonable since the reaction was carried out under the reducing atmosphere at a relatively high temperature (650 °C). It is evident that the addition of a mild oxidant CO₂ can replenish the reducible oxygen species on the catalyst surface, thus stabilizing the activity during the dehydrogenation.

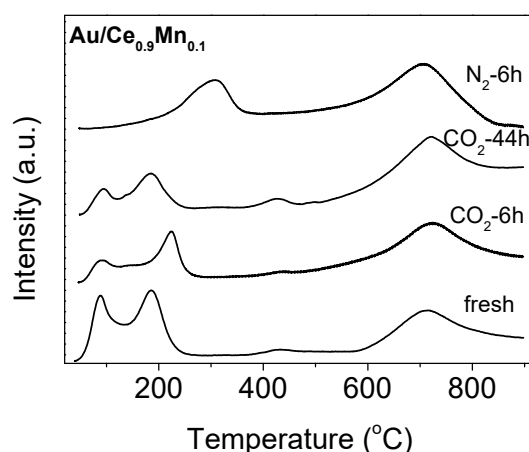


Figure 7. TPR profiles of fresh and spent Au/Ce_{0.9}Mn_{0.1} catalysts.

3. Materials and Methods

3.1. Catalyst Preparation

The Mn-doped CeO₂ nanorod was synthesized by a modified hydrothermal method following the procedure in the literature [36]. Typically, the calculated amount of Ce(NO₃)₃·6H₂O and 50 wt% Mn(NO₃)₂ solution were dissolved in 20 mL deionized water; 38.4 g NaOH was dissolved in another 140 mL of deionized water. The above two solutions were then mixed and kept stirring for 30 min to form a slurry. The slurry was transferred into a Teflon-lined stainless-steel autoclave and subjected to hydrothermal treatment for 24 h at 100 °C. The obtained precipitates were recovered by filtration, washed thoroughly with deionized water, dried at 100 °C and finally calcined at 450 °C for 3 h. These materials were denoted as Ce_{1-x}Mn_xO_{2-δ} while x represents the molar ratio of Mn/(Ce+Mn).

Deposition of Au was prepared by a deposition-precipitation (DP) method. The Ce_{1-x}Mn_xO_{2-δ} solid was dispersed in an aqueous solution of HAuCl₄ at a fixed pH of 7.5. The Au loading was 1.0 wt%. The suspension was aged at room temperature for 24 h and then washed with deionized water. After being dried at 100 °C, these Au-containing materials were calcined in air at 650 °C for 6 h, and denoted as Au/Ce_{1-x}Mn_xO_{2-δ}.

3.2. Catalyst Characterizations

X-ray powder diffraction (XRD) patterns were recorded on Persee XD-2 X-ray diffractometer (Persee, Beijing, China) using nickel-filtered Cu K α radiation at 40 kV and 30 mA. X-ray photoelectron spectra (XPS) were obtained by using Mg K α radiation on a Perkin-Elmer PHI 5000C spectrometer (Perkin-Elmer, Boston, MA, USA). The BET surface areas of the catalysts were analyzed by N₂ adsorption at -196 °C using a Micromeritics ASAP 2000 instrument (Micromeritics, Atlanta, GA, USA). Transmission electron microscopy (TEM) images were recorded on a JEOL 2011 electron microscope (JEOL, Tokyo, Japan) operating at 200 kV. Temperature-programmed reduction (H₂-TPR) was carried out on a Micromeritics AutoChem II apparatus (Micromeritics, Atlanta, GA, USA) loaded with 100 mg of catalyst under a 10 vol% H₂/Ar flowing gas (30 mL/min), with a ramping rate of 10 °C/min. The consumption of H₂ was monitored using a thermal conductivity detector. Laser Raman spectra were obtained on a Horiba JY XPloRA spectrometer (HORIBA, Tyoto, Japan) using the 532 nm radiation of an air-cooled solid state laser as an excitation source.

3.3. Catalyst Evaluation

Catalytic tests for ethane dehydrogenation were performed at 650 °C in a fixed-bed flow microreactor at atmospheric pressure. The catalyst load was 200 mg, and it was activated at 650 °C for 2 h in nitrogen flow prior to the reaction. Typically, the gas reactant contained 3 vol% ethane,

15 vol% CO₂ and the balance nitrogen. For reactions carried out in the absence of CO₂, the gas reactant contained 3 vol% ethane and the balance nitrogen. The total flow rate of the gas reactant is 30 mL/min. The hydrocarbon reaction products were analyzed using an on-line GC equipped with a 6 m packed column of Porapak Q and a FID. The gas products, such as N₂, CO and CO₂, were analyzed on-line by another GC equipped with a 2 m packed column of carbon molecular sieve 601 and a TCD. The reaction data in the work were reproducible with a precision of less than 5%.

4. Conclusions

The catalytic dehydrogenation of ethane to ethylene was conducted in the presence of CO₂ over Mn-doped ceria nanorod-supported Au catalysts. The initial ethane conversion was enhanced with the Mn doping. XPS analysis showed the predominated Mn³⁺ fraction in the Au/Ce_{1-x}Mn_xO_{2-δ} catalysts and a monotonously decreased Ce³⁺ concentration with the doping of Mn, suggesting that the doped Mn might preferentially occupy the defect sites of CeO₂ crystals and cause the formation of extra oxide ions. The TPR measurement showed that the consumed hydrogen attributing to the ceria species of the Au/Ce_{1-x}Mn_xO_{2-δ} catalysts shared a similar sequence with the DHE performance, indicating that these reducible oxygen species-related ceria might play a vital role in the dehydrogenation.

The addition of CO₂ slightly promoted the initial activity but greatly improved the stability of Au/Ce_{0.9}Mn_{0.1} by eliminating the carbonaceous deposits through the Boudouard reaction and sustainably supplementing the reducible oxygen specie on the surface. The long-time test showed that Mn-doped CeO₂ nanorod-supported Au is a promising catalyst for ethane dehydrogenation in the presence of CO₂. A steady ethane conversion of 17.4% with an ethylene selectivity of 97.5% can be obtained.

Supplementary Materials: The following are available online at <http://www.mdpi.com/2073-4344/9/2/119/s1>, Figure S1: XPS spectra of the Au/Ce_{1-x}Mn_xO_{2-δ} catalysts, Figure S2: Deconvolution of the TPR profiles of the Au/Ce_{1-x}Mn_xO_{2-δ} catalysts, Figure S3: Raman profiles of the spent Au/Ce_{0.9}Mn_{0.1} catalysts.

Author Contributions: Y.Y. conceived and designed the experiments; T.L. and H.G. performed the experiments; W.H., C.M. and Z.G. analyzed the data; T.L. wrote the paper; W.H., C.M. and Y.Y. revised the paper.

Funding: This research was funded by the National Key R&D Program of Ministry of Science and Technology, grant number 2017YFB0602204, National Natural Science Foundation of China, grant number 91645201 and the Science & Technology Commission of Shanghai Municipality (13DZ2275200).

Conflicts of Interest: The authors declare no conflict of interest.

References

1. Nawaz, Z. Light alkane dehydrogenation to light olefin technologies: A comprehensive review. *Rev. Chem. Eng.* **2015**, *31*, 413–436. [CrossRef]
2. Sattler, J.J.H.B.; Ruiz-Martinez, J.; Santillan-Jimenez, E.; Weckhuysen, B.M. Catalytic dehydrogenation of light alkanes on metals and metal oxides. *Chem. Rev.* **2014**, *114*, 10613–10653. [CrossRef] [PubMed]
3. Wang, S.B.; Zhu, Z.H. Catalytic conversion of alkanes to olefins by carbon dioxide oxidative dehydrogenation. *Energy Fuel* **2004**, *18*, 1126–1139. [CrossRef]
4. Ansari, M.B.; Park, S.E. Carbon dioxide utilization as a soft oxidant and promoter in catalysis. *Energy Environ. Sci.* **2012**, *5*, 9419–9437. [CrossRef]
5. Mukherjee, D.; Park, S.E.; Reddy, B.M. CO₂ as a soft oxidant for oxidative dehydrogenation reaction: An eco benign process for industry. *J. CO₂ Util.* **2016**, *16*, 301–312. [CrossRef]
6. Atanga, M.A.; Rezaei, F.; Jawad, A.; Fitch, M.; Rowanaghi, A.A. Oxidative dehydrogenation of propane to propylene with carbon dioxide. *Appl. Catal. B* **2018**, *220*, 429–445. [CrossRef]
7. Nakagawa, K.; Okamura, M.; Ikenaga, N.; Suzuki, T.; Kobayashi, T. Dehydrogenation of ethane over gallium oxide in the presence of carbon dioxide. *Chem. Commun.* **1998**, 1025–1026. [CrossRef]
8. Nakagawa, K.; Kajita, C.; Okumura, K.; Ikenaga, N.; Nishitani-Gamo, M.; Ando, T.; Kobayashi, T.; Suzuki, T. Role of carbon dioxide in the dehydrogenation of ethane over gallium-loaded catalysts. *J. Catal.* **2001**, *203*, 87–93. [CrossRef]

9. Cheng, Y.H.; Lei, T.Q.; Miao, C.X.; Hua, W.M.; Yue, Y.H.; Gao, Z. Ga₂O₃/NaZSM-5 for C₂H₆ dehydrogenation in the presence of CO₂: Conjugated effect of silanol. *Microporous Mesoporous Mater.* **2018**, *268*, 235–242. [[CrossRef](#)]
10. Cheng, Y.H.; Miao, C.X.; Hua, W.M.; Yue, Y.H.; Gao, Z. Cr/ZSM-5 for ethane dehydrogenation: Enhanced catalytic activity through surface silanol. *Appl. Catal. A* **2017**, *532*, 111–119. [[CrossRef](#)]
11. Lei, T.Q.; Miao, C.X.; Hua, W.M.; Yue, Y.H.; Gao, Z. Silica-doped TiO₂ as support of gallium oxide for dehydrogenation of ethane with CO₂. *Fuel Process. Technol.* **2018**, *177*, 246–254. [[CrossRef](#)]
12. Tóth, A.; Halasi, G.; Solymosi, F. Reactions of ethane with CO₂ over supported Au. *J. Catal.* **2015**, *330*, 1–5. [[CrossRef](#)]
13. Tóth, A.; Halasi, G.; Bánsági, T.; Solymosi, F. Reactions of propane with CO₂ over Au catalysts. *J. Catal.* **2016**, *337*, 57–64. [[CrossRef](#)]
14. Lei, T.Q.; Miao, C.X.; Hua, W.M.; Yue, Y.H.; Gao, Z. Oxidative dehydrogenation of ethane with CO₂ over Au/CeO₂ Nanorod catalysts. *Catal. Lett.* **2018**, *148*, 1634–1642. [[CrossRef](#)]
15. Zhang, L.; Wu, Z.; Nelson, N.C.; Sadow, A.D.; Slowing, I.I.; Overbury, S.H. Role of CO₂ as a soft oxidant for dehydrogenation of ethylbenzene to styrene over a high-surface-area ceria catalyst. *ACS Catal.* **2015**, *5*, 6426–6435. [[CrossRef](#)]
16. Yao, H.C.; Yao, Y.F.Y. Ceria in automotive exhaust catalysts: I. Oxygen storage. *J. Catal.* **1984**, *86*, 254–265. [[CrossRef](#)]
17. Lu, J.L.; Gao, H.J.; Shaikhutdinov, S.; Freund, H.J. Gold supported on well-ordered ceria films: Nucleation, growth and morphology in CO Oxidation reaction. *Catal. Lett.* **2007**, *114*, 8–16. [[CrossRef](#)]
18. Reina, T.R.; Ivanova, S.; Centeno, M.A.; Odriozola, J.A. The role of Au, Cu & CeO₂ and their interactions for an enhanced WGS performance. *Appl. Catal. B* **2016**, *187*, 98–107.
19. Zhen, J.; Wang, X.; Liu, D.; Song, S.; Wang, Z.; Wang, Y.; Li, J.; Wang, F.; Zhang, H. Co₃O₄@CeO₂ Core@Shell Cubes: Designed synthesis and optimization of catalytic properties. *Chem. Eur. J.* **2014**, *20*, 4469–4473. [[CrossRef](#)] [[PubMed](#)]
20. Su, Y.; Wang, S.; Zhang, T.; Wang, S.; Zhu, B.; Cao, J.; Yuan, Z.; Zhang, S.; Huang, W.; Wu, S. Comparative study on catalytic performances for low-temperature CO oxidation of Cu-Ce-O and Cu-Co-Ce-O catalysts. *Catal. Lett.* **2008**, *124*, 405–412. [[CrossRef](#)]
21. Qi, G.S.; Yang, R.T.; Chang, R. MnOx-CeO₂ mixed oxides prepared by co-precipitation for selective catalytic reduction of NO with NH₃ at low temperatures. *Appl. Catal. B* **2004**, *51*, 93–106. [[CrossRef](#)]
22. Delimaris, D.; Loannides, T. VOC oxidation over MnOx-CeO₂ catalysts prepared by a combustion method. *Appl. Catal. B* **2008**, *84*, 303–312. [[CrossRef](#)]
23. Venkataswamy, P.; Jampaiah, D.; Mukherjee, D.; Aniz, C.U.; Reddy, B.M. Mn-doped ceria solid solutions for CO oxidation at lower temperatures. *Catal. Lett.* **2016**, *146*, 2105–2118. [[CrossRef](#)]
24. Chen, H.Y.; Sayai, A.; Adnot, A.; Larahi, F. Composition-activity effects of Mn-Ce-O composites on phenol catalytic wet oxidation. *Appl. Catal. B* **2001**, *32*, 195–204. [[CrossRef](#)]
25. Si, R.; Flytzani-Stephanopoulos, M. Shape and crystal-plane effects of nanoscale ceria on the activity of Au-CeO₂ catalysts for the water-gas shift reaction. *Angew. Chem. Int. Ed.* **2008**, *47*, 2884–2887. [[CrossRef](#)] [[PubMed](#)]
26. Huang, X.S.; Sun, H.; Wang, L.C.; Liu, Y.M.; Fan, K.N.; Cao, Y. Morphology effects of nanoscale ceria on the activity of Au/CeO₂ catalysts for low-temperature CO oxidation. *Appl. Catal. B* **2009**, *90*, 224–232. [[CrossRef](#)]
27. Hong, W.J.; Iwamoto, S.; Hosokawa, S.; Wada, K.; Kanai, H.; Inoue, M. Effects of Mn content on physical properties of CeOx-MnOy support and BaO-CeOx-MnOy catalysts for direct NO decomposition. *J. Catal.* **2011**, *277*, 208–216. [[CrossRef](#)]
28. Liyanage, A.D.; Perera, S.D.; Tan, K.; Chabal, Y.; Balkus, K.J. Synthesis, characterization, and photocatalytic activity of Y-doped CeO₂ nanorods. *ACS Catal.* **2014**, *4*, 577–584. [[CrossRef](#)]
29. Gao, T.; Norby, P.; Krumeich, F.; Okamoto, H.; Nesper, R.; Fjellvag, H. Synthesis and properties of layered-structured Mn₅O₈ nanorods. *J. Phys. Chem. C* **2010**, *114*, 922–928. [[CrossRef](#)]
30. Larachi, F.; Pierre, J.; Adnot, A.; Bernis, A. Ce 3d XPS study of composite Ce_xMn_{1-x}O_{2-y} wet oxidation catalysts. *Appl. Surf. Sci.* **2002**, *195*, 236–250. [[CrossRef](#)]
31. Park, E.D.; Lee, J.S. Effects of pretreatment conditions on CO oxidation over supported Au catalysts. *J. Catal.* **1999**, *186*, 1–11. [[CrossRef](#)]

32. Tang, X.F.; Chen, J.L.; Li, Y.G.; Xu, Y.D.; Shen, W.J. Complete oxidation of formaldehyde over Ag/MnO_x-CeO₂ catalysts. *Chem. Eng. J.* **2006**, *118*, 119–125. [[CrossRef](#)]
33. Venezia, A.M.; Pantaleo, G.; Longo, A.; Carlo, G.D.; Casaletto, M.P.; Liotta, F.L.; Deganello, G. Relationship between structure and CO oxidation activity of ceria-supported gold catalysts. *J. Phys. Chem. B* **2005**, *109*, 2821–2827. [[CrossRef](#)]
34. Zhang, S.H.; Muratsugu, S.; Ishiguro, N.; Tada, M. Ceria-doped Ni/SBA-16 catalysts for dry reforming of methane. *ACS Catal.* **2013**, *3*, 1855–1864. [[CrossRef](#)]
35. Lan, G.J.; Tang, H.D.; Zhou, Y.P.; Han, W.F.; Liu, H.Z.; Li, X.N.; Li, Y. Direct synthesis of ruthenium-containing ordered mesoporous carbon with tunable embedding degrees by using a boric acid-assisted approach. *ChemCatChem* **2014**, *6*, 353–360. [[CrossRef](#)]
36. Mai, H.X.; Sun, L.D.; Zhang, Y.W.; Si, R.; Feng, W.; Zhang, H.P.; Liu, H.C.; Yan, C.H. Shape-selective synthesis and oxygen storage behavior of ceria nanopolyhedra, nanorods, and nanocubes. *J. Phys. Chem. B* **2005**, *109*, 24380–24385. [[CrossRef](#)]



© 2019 by the authors. Licensee MDPI, Basel, Switzerland. This article is an open access article distributed under the terms and conditions of the Creative Commons Attribution (CC BY) license (<http://creativecommons.org/licenses/by/4.0/>).